

Models of the iron K_α fluorescence line and the Compton shoulder in irradiated accretion disk spectra

A. Róžańska^{1*}, J. Madej^{2*}

¹ Copernicus Astronomical Center, Bartycka 18, 00-716 Warsaw, Poland

² Warsaw University Observatory, Al. Ujazdowskie 4, 00-478 Warsaw, Poland

Accepted

ABSTRACT

We present a full set of model atmosphere equations for the accretion disk around a supermassive black hole irradiated by hard X-ray lamp of power-law spectral distribution. Model equations allow for multiple Compton scattering of radiation on free electrons, and for large relative photon-electron energy exchange at the time of scattering. We present spectra in specific intensities integrated over the disk surface. Theoretical outgoing intensity spectra show soft X-ray excess below 1 keV, and distinct K_α and K_β fluorescent lines of iron. We demonstrate the existence of the Compton Shoulder and claim that it can contribute to the asymmetry and equivalent widths of some observed Fe K_α lines in AGN. Our models exhibit the effect of limb-brightening in reflected X-rays.

Key words: accretion disks - galaxies: active - radiative transfer - scattering - line: profiles

1 INTRODUCTION

Observations of many active galactic nuclei (AGN) directly show the existence of an X-ray source in the innermost region of AGN, which emits radiation with power-law spectrum extending to above 100 keV (Guainazzi et al. 1999; Done et al. 2003). The exact location of the source is still unclear, nevertheless, such hard radiation strongly affects other emitting regions including nearby accretion disk. Effects of the redistribution of hard X-rays into the soft X-ray and ultraviolet domains are frequently observed in many AGN starting with the paper Pounds et al. (1990) up to the recent paper Nandra & Iwasawa (2007).

The most important spectral feature indicating that the reflection occurs from an accretion disk, is a fluorescent iron K_α line. Close to the supermassive black hole, the emission iron line profile is relativistically broadened and skewed (Fabian et al. 1989; Reynolds & Begelman 1997), which together with a circular gas movement in a disk, makes final profile asymmetric with a strong red wing.

The detection of iron line profile was a goal of several X-ray satellites, and the results depend on the resolution of a particular instrument. The best known object with broad iron K_α line, MCG-6-30-15 was observed by *ASCA* (Tanaka et al. 1995; Iwasawa et al. 1999). In the *Chandra* and *XMM* era, line became narrow or contained both broad and narrow component (Reeves et al. 2004;

Petrucci et al. 2007). Recently, more often authors are reporting a detection of “iron line complex” additionally affected by intrinsic warm absorber (Yaqoob & Padmanabhan 2004; Risaliti et al. 2005; Matt et al. 2006).

The most recent data coming from *Suzaku* look very promising (Miniutti et al. 2007; Reeves et al. 2007; Yaqoob et al. 2007). The iron line complex contains at least two components: narrow Gaussian at 6.4 keV, and broad red wing, the last one usually fitted with a disk like shape, but also with Compton shoulder in the work of Reeves et al. (2007). Additionally iron K_β line at energy 7.057 keV is clearly seen in *Suzaku* AGN (Reeves et al. 2007; Markowitz et al. 2007; Yaqoob et al. 2007).

In this paper we present quite consistent and numerically exact modeling of the iron line complex originating from an accretion disk atmosphere irradiated by hard X-rays with power-law spectral distribution. Our computations of the vertical structure and outgoing spectrum of the disk are based on rigorous method of the theory of stellar atmospheres (Madej 1991; Madej & Róžańska 2000a,b). All existing opacity sources both true absorption and Compton scattering are treated equivalently in the single code fully described in Madej & Róžańska (2004, hereafter MR04). Adopting atmospheric computations for an accretion disk around supermassive black hole, we solve the structure and obtain outgoing spectra for eight neighboring rings. The final spectrum presented in specific intensity scale for different aspect angles is integrated over radii and presented at

* E-mail: agata@camk.edu.pl (AR); jm@astrouw.edu.pl (JM)

the source frame. No kinematic special relativity effects are included in our model.

Our radiative transfer equation includes effects of multiple Compton scattering of radiation on free electrons in relativistic thermal motion, and rich set of bound-free and free-free opacities. We allow for a large relative photon-electron energy exchange at the time of Compton scattering and, therefore, are able to reconstruct Compton scattering of photons with energy approaching or even exceeding the electron rest mass. In this paper the opacities are supplemented by formulae describing emission of fluorescent K_α and K_β lines of low ionized iron.

The structure of the paper is as follows: Sec. 2 describes sample accretion disk model, and Sec. 3 presents most important equations used in our code. Results are presented in Sec. 4 and Sec. 5 and summarized in Sec. 6 and Sec. 7.

2 MODEL OF A SAMPLE ACCRETION DISK

We consider an exemplary model of the accretion disk around supermassive black hole located at the center of AGN. Mass of the black hole equals $M_{BH} = 10^7 M_\odot$. We divide our disk onto 8 concentric rings situated at different distances from the center. We assume constant moderate value of accretion rate in each ring, equal $\dot{m} = 0.03$ in units of Eddington accretion rate with accreting efficiency $\eta = 1/12$ suitable for the Schwarzschild black hole.

At the first step, at each radius, we computed vertical structure of non-irradiated disk using the method described in Różańska et al. (1999). We integrated equations of the disk vertical structure (equation of the hydrostatic equilibrium, equation of state, equation of local energy generation, transfer in diffusion approximation) assuming that viscosity is proportional to the total pressure, i.e. $P_{tot} = P_{rad} + P_{gas}$. As the result, for each ring, we derived effective temperature and vertical gravity which affects atmosphere, and we adopted them for actual computations. All disk parameters used in further computations are summarized in Tab. 1 column 3 and 4.

At the next step, we assume that the disk is irradiated by an external point like X-ray lamp, located above the first innermost ring, $r_1 = 3.48 r_{Schw}$, at the height $h_l = 5 r_{Schw}$. Irradiation spectrum is in the form of power-law with exponential low and high energy cut-off (see Sec. 3.1.2).

The code by Różańska et al. (1999) predicted the value of gravity, $\log g_m$, for each ring of the non-irradiated disk. When external irradiation was applied, the atmosphere always lost its hydrostatic equilibrium. We had to increase the value of surface gravity by a factor of two or more to restore hydrostatic equilibrium in those rings, where equilibrium probably may not exist. There is no firm physical justification for such a step, of course. Values of gravity adopted for the advanced radiative transfer computations, $\log g_{irr}$, are listed in the fifth column of Tab. 1.

We take into account three different chemical compositions of the accretion disk presented in Table 2. The first composition, Comp. I, consists only of hydrogen, helium and iron in proportions close to solar values. Comp. II is just the solar chemical composition for only ten most abundant elements given by Chaisson & McMillan (1996). We also con-

Table 1. Parameters of the disk for $M_{BH} = 10^7 M_\odot$, $\dot{m} = 0.03$.

ring No.	r/r_{Schw}	T_{eff}	$\log g_m$	$\log g_{irr}$
1	3.478E+00	1.018E+05	5.230E+00	5.5300
2	4.134E+00	1.073E+05	5.274E+00	5.5740
3	5.204E+00	1.020E+05	5.170E+00	5.4700
4	6.552E+00	9.238E+04	5.001E+00	5.3010
5	8.248E+00	8.181E+04	4.801E+00	5.1010
6	1.038E+01	7.152E+04	4.582E+00	5.1820
7	1.385E+01	5.976E+04	4.294E+00	5.594
8	1.847E+01	4.950E+04	3.996E+00	5.596

Table 2. Three chemical compositions used in our calculations. Entries of the table display number abundances of elements relative to hydrogen. Three rows at the bottom present mass abundances X, Y, and Z for all three composition.

	Comp. I	Comp. II	Comp. III
H	1.0	1.0	1.0
He	1.1×10^{-1}	9.54×10^{-2}	9.54×10^{-2}
C	-	4.72×10^{-4}	4.72×10^{-4}
N	-	9.65×10^{-5}	9.65×10^{-5}
O	-	8.55×10^{-4}	8.55×10^{-4}
Ne	-	3.84×10^{-5}	3.84×10^{-5}
Mg	-	4.17×10^{-5}	4.17×10^{-5}
Si	-	4.94×10^{-5}	4.94×10^{-5}
S	-	1.64×10^{-5}	1.64×10^{-5}
Fe	3.7×10^{-5}	3.29×10^{-5}	6.58×10^{-5}
X	0.695	0.712	0.711
Y	0.304	0.270	0.269
Z	2.066×10^{-2}	2.624×10^{-2}	2.808×10^{-2}

sidered the model of solar composition with doubled number abundance of iron named as Comp. III.

In this paper, we have calculated our canonical model of the disk with chemical composition Comp. I, and the power-law irradiation with spectral index $\alpha_X = 0.9$, and X-ray luminosity $L_X = 10^{43}$ erg s⁻¹. For chemical composition, Comp. I, we compared this canonical model to the case of power-law with the same spectral index, but different luminosities: $L_X = 10^{42}$ erg s⁻¹ and $L_X = 10^{44}$ erg s⁻¹, and to the case of power-law with the same luminosity but different spectral indices: $\alpha_X = 0.6$ and $\alpha_X = 1.2$. We also compared the structure and spectrum of our canonical model to models with the luminosity $L_X = 10^{43}$ erg s⁻¹, and spectral index $\alpha_X = 0.9$, but with other chemical compositions: Comp. II and Comp. III. In all computed models the power-law radiation extends between $h\nu_{min} = 0.1$ and $h\nu_{max} = 100$ keV.

3 EQUATIONS OF AN IRRADIATED ATMOSPHERE

The set of equations presented and solved here represents a direct extension of the equations presented in MR04. Now we added terms which correspond to the fluorescent K_α and K_β lines of iron, adjusted to the accretion disk geometry and assumed that the external irradiation from a point X-ray lamp has the power-law spectral distribution.

3.1 The equation of transfer

The equation of transfer for the specific intensity I_ν at frequency ν was written in plane-parallel geometry on the geometrical depth scale z

$$\mu \frac{dI_\nu}{\rho dz} = j_\nu - (\kappa_\nu + \sigma_\nu)I_\nu, \quad (1)$$

where j_ν , κ_ν and σ_ν denote frequency dependent emission, absorption and scattering coefficients for 1 gram, respectively. In this paper we use the LTE (local thermodynamic equilibrium) absorption κ_ν , whereas coefficients of emission j_ν and scattering σ_ν include nonLTE terms.

Eq. 1 can be written on the monochromatic optical depth, with $d\tau_\nu = -(\kappa_\nu + \sigma_\nu)\rho dz$, then

$$\mu \frac{dI_\nu}{d\tau_\nu} = I_\nu - \frac{j_\nu}{\kappa_\nu + \sigma_\nu} = I_\nu - S_\nu, \quad (2)$$

where S_ν is the frequency dependent source function.

Emission coefficient j_ν is the sum of three terms, $j_\nu = j_\nu^{th} + j_\nu^{sc} + j_\nu^{fl}$, which represent thermal emission, Compton scattering emission and the emission in iron fluorescent lines, respectively.

3.1.1 Thermal emission

Coefficient of thermal emission j_ν in LTE is proportional to the Planck function B_ν

$$j_\nu^{th} = \kappa_\nu B_\nu. \quad (3)$$

The coefficient of true absorption κ_ν , is the sum of bound-free absorption from numerous levels of atoms and ions for all elements, plus free-free absorption from all ions.

We also included absorption of 4 lowest lines of fundamental series of helium-like iron and of similar 4 lowest lines of hydrogen like iron, all formed in LTE by assumption.

3.1.2 External irradiation

We defined two angle-averaged variables, which were derived from the specific intensity I_ν^{ext} of the external irradiation penetrating the atmosphere to the depth τ_ν

$$U_\nu(\tau_\nu) = \frac{1}{4\pi} \int_\Omega I_\nu^{ext}(\omega, \tau_\nu) \exp(-\tau_\nu/\mu_\omega) d\omega, \quad (4)$$

$$J_\nu(\tau_\nu) = \frac{1}{4\pi} \int_\Omega I_\nu^{ext}(\omega, \tau_\nu) \mu_\omega \exp(-\tau_\nu/\mu_\omega) d\omega, \quad (5)$$

where μ_ω stands for the cosine of zenithal angle of the running direction ω . The external intensity from the point-like lamp is emitted in the form of power-law with spectral index α_X :

$$I_\nu^{ext} = A \nu^{-\alpha_X} \exp\left(-\frac{\nu}{\nu_{max}}\right) \exp\left(-\frac{\nu_{min}}{\nu}\right), \quad (6)$$

and normalized to the luminosity of the source, L_X :

$$A = \frac{L_X}{4\pi r_i^2 \left[\int_{\nu_{min}}^{\nu_{max}} \nu^{-\alpha_X} \exp\left(-\frac{\nu}{\nu_{max}}\right) \exp\left(-\frac{\nu_{min}}{\nu}\right) d\nu \right]}. \quad (7)$$

The distance from an X-ray source depends on the ring radius r in the casual relation $r_i^2 = h_i^2 + r^2$. The luminosity, spectral index, and cut-off limits of irradiating spectrum are free parameters of our model, all of them described in Sec. 2.

3.1.3 Compton scattering emission

Expressions for the Compton scattering terms and emission coefficient in an irradiated stellar atmosphere were derived in MR04 and are valid in a disk atmosphere without any changes

$$j_\nu^{sc} = \sigma_\nu J_\nu - \sigma_\nu J_\nu \int_0^\infty \Phi_1(\nu, \nu') d\nu' + \sigma_\nu \int_0^\infty (J_{\nu'} + U_{\nu'}) \Phi_2(\nu, \nu') d\nu'. \quad (8)$$

In the above equation variable U_ν denotes the angle-averaged intensity of the external irradiation (Eq. 4).

Compton scattering cross sections were computed following the paper by Guilbert (1981). Functions Φ_1 and Φ_2 are properly weighted angle-averaged Compton redistribution functions for photons both incoming or outgoing of frequency ν after scattering in thermal electron gas, cf. MR04.

3.1.4 Iron fluorescence emission

Fluorescence of low-ionized iron gas was approximated by two emission lines, K_α and K_β . Therefore,

$$j_\nu^{fl} = E_\alpha^{fl} \varphi_\nu^\alpha + E_\beta^{fl} \varphi_\nu^\beta, \quad (9)$$

where E_α^{fl} and E_β^{fl} denote the integrated intensity of K_α and K_β emission lines, respectively. Frequency dependent variables φ_ν^α and φ_ν^β define profiles of fluorescent lines, both normalized to unity.

Energy emitted in K_α and K_β lines was derived by absorption of hard continuum X-rays from the radiation field penetrating the disk atmosphere. Hard X-ray photon interacting with neutral or low-ionized iron most probably ionize and remove electron from the innermost K shell, and then remaining hole is filled by another electron falling from L shell (K_α) or M shell (K_β transition). The integrated emissivity for Fe K_α fluorescent line is given by:

$$E_\alpha^{fl} = Y \times h\nu_0 \int_{\nu_0}^\infty \frac{\alpha_\nu^{\text{iron}}}{h\nu} (J_\nu + U_\nu) d\nu, \quad (10)$$

where we set $Y = 0.34$ (Krause & Oliver 1979). Variable α_ν^{iron} is the bound-free absorption coefficient for ionization from K shell of iron counted for 1 atom. Similar expression holds for the integrated intensity E_β^{fl} .

The fluorescence yield, Y , defines the fraction of the energy of hard X-rays absorbed by iron atoms which was reemitted as photons in K_α line. The remaining energy of absorbed X-rays, $1 - Y$, was spent for the release of Auger electrons.

The iron K_α fluorescent line is a doublet line, and such a structure was reproduced by our code. We set the central energies for K_{α_1} and K_{α_2} lines to 6.404 keV and 6.391 keV, respectively. Natural widths (FWHM) of both lines, 2.7 eV (K_{α_1}) and 3.3 eV (K_{α_2}) were taken from Krause & Oliver (1979). The K_β line was approximated by a singlet line at the energy 7.057 keV. We set the natural width of the line to 2.5 eV arbitrarily.

Integrated emissivity E_α^{fl} was divided in the proportion 2:1 between K_{α_1} and K_{α_2} components of the doublet. Following Basko (1978) we quite arbitrarily assumed that the integrated intensity $E_\beta^{fl} = 0.1 E_\alpha^{fl}$. Opacity profiles of all

three lines were set to Voigt functions with depth-dependent parameters describing natural and thermal broadening.

3.2 Equation of state

We used here the LTE equation of state, where the number of free electrons and all ionization populations of iron was determined by the Saha ionization equations.

In the case of an atmosphere irradiated by strong non-local radiation field the assumption of LTE yields inaccurate ionization and excitation populations. For instance we get inaccurate populations of iron atoms with various configurations of electrons in the outermost M and N shells.

This is the reason that we did not discuss in our paper intensities for the spectral features of energies below the soft X-ray excess in the outgoing spectra, where the nonLTE configuration of outermost bound electrons in various atoms is of vital importance.

However, we believe that the population of iron atoms with filled innermost K and L shells is always equal to the total number of iron atoms with 8 or more bound electrons, and does not depend on the LTE/nonLTE details of electron populations in M and N shells. As the result we believe that have obtained reasonable intensities for both fluorescent lines K_α and K_β of low-ionized iron. The lines were considered strictly in nonLTE.

3.3 Equations of hydrostatic and radiative equilibrium

3.3.1 Hydrostatic equilibrium

We solve the static equation of equilibrium for gas pressure:

$$\frac{dP_{gas}}{d\tau} = \frac{g}{(\kappa + \sigma)_{std}} - \frac{dP_{rad}}{d\tau}, \quad (11)$$

which takes into account gradient of radiation pressure P_r at the level τ . Expanded form of the equation is

$$\frac{dP_{gas}}{d\tau} = \frac{g}{(\kappa + \sigma)_{std}} - \frac{4\pi}{c} \int_0^\infty \eta_\nu (H_\nu - V_\nu) d\nu, \quad (12)$$

where $\eta_\nu = (\kappa_\nu + \sigma_\nu)/(\kappa + \sigma)_{std}$. Eq. 12 neglects possible vertical motion of matter which can be caused by the differential rotation of the disk.

In addition we assumed that the vertical gravitational acceleration in the atmosphere of a given ring is constant i.e. its dependence on the height above the disk equatorial plane was neglected. The value of acceleration was computed from the solution of the disk model presented in Sec. 2.

3.3.2 Radiative equilibrium

Constraint of radiative equilibrium requires that

$$\int_0^\infty H_\nu(\tau_\nu) d\nu - \int_0^\infty V_\nu(\tau_\nu) d\nu = \frac{\sigma_R T_{\text{eff}}^4}{4\pi} \quad (13)$$

at each depth level of τ_ν in the atmosphere. Radiative constant $\sigma_R = 5.66961 \times 10^{-5}$ (cgs units). In this paper, we assumed that whole flux from an accretion disk was generated below an atmosphere, and we do not solve local energy generation via viscosity.

The above equation subsequently was used to determine distribution of temperature in the disk atmosphere at a given ring. Transformation of Eq. 13 to the expression for temperature corrections δT was done by the linearization technique. The equation of transfer including temperature corrections was solved using the technique of variable Eddington factors (Mihalas 1978). Details of the full set of equations used in our computations and the method of solution by partial linearization are presented in MR04.

4 COMPUTATIONAL RESULTS

Our computer code allowed us to compute the structure of disk atmospheres over very large range of electron scattering optical depth starting from $\tau_{es} = 10^{-8}$ up to $\tau_{es} = 10^5$. Furthermore, we were able to reproduce the overall continuum spectrum from deep infrared of 0.4 eV up to hard X-rays of 400 keV. We present our spectra as an energy dependent outgoing specific intensities, I_ν , which are suitable for disk geometry. We reject presentation of monochromatic fluxes since they are relevant only to geometry of a spherical star.

4.1 Temperature structure

Fig. 1 represents the temperature structure of various irradiated models. The canonical model for several rings is presented in panel (a). In panel (b) our canonical model is compared with models of the same spectral index, but with different X-ray luminosities, while in panel (c) with models of the same X-ray luminosity but with different spectral indices. Panel (d) shows the structure of the disk irradiated by the power-law with $\alpha_X = 0.9$ and luminosity $L_X = 10^{43}$ erg s⁻¹ but for various chemical compositions. In panels (b), (c), (d) we show temperature structure only for the innermost ring number 1.

In all computed cases we note the existence of very hot outermost atmospheric layer which is caused by external irradiation (Nayakshin et al. 2000; Ballantyne et al. 2001; Hubeny et al. 2001; Różańska et al. 2002). The effective temperature of all rings resulted from the accretion rate and non-zero viscosity, is slightly less or equal to 10^5 K. However, the temperature of the outermost hot skin approaches 3×10^6 K. For deeper layers external irradiation practically does not change the temperature of the gas.

The surface temperature is determined by the balance between Compton heating caused by hard X-ray photons from the external illumination and inverse Compton cooling by the low-energy reprocessed radiation and thermal radiation from the disk below. Hence the actual surface temperature is lower than the Compton temperature due to the illumination alone.

In our canonical model, the temperature of the hot skin is almost the same for all rings (panel (a)) and apparently it does not change with the distance from the central black hole for a given power-law hardness and the luminosity of the external irradiation. We demonstrate, that the surface temperature depends on the X-ray luminosity (panel (b)) and the hardness of spectrum (panel (c)). For softer power-law, $\alpha_X = 1.2$, Compton heated skin has lower temperature, but transition from hot to colder layer occurs deeper in the atmosphere (long dashed line in panel (c)).

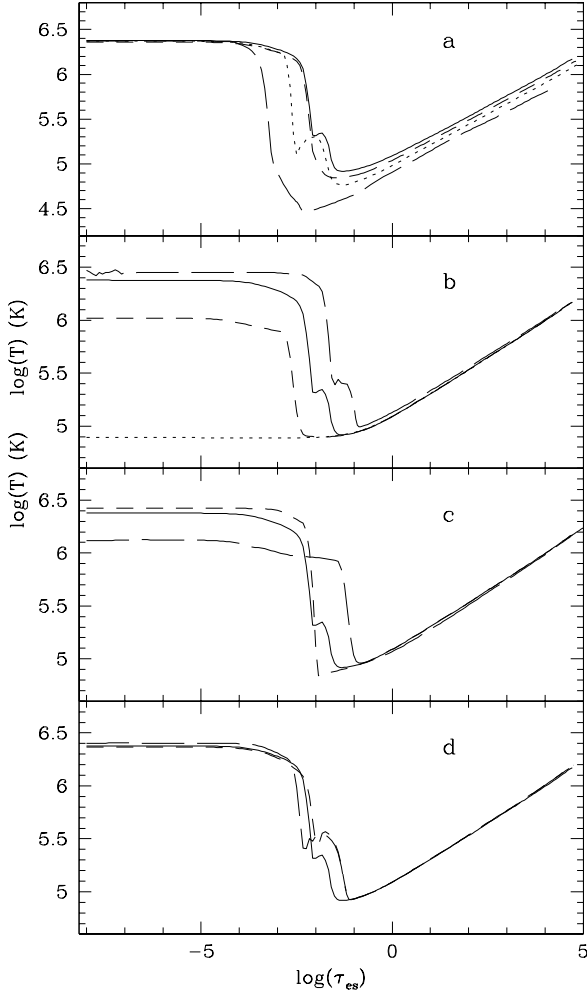


Figure 1. Comparison of temperature structure for different models. In panel (a) our canonical model is presented for ring 1 - solid line, ring 4 - short-dashed line, ring 5 - dotted line, and ring 8 - long-dashed line. In panel (b) canonical model (solid line), is compared with models of different luminosities: $L_X = 10^{44}$ erg s^{-1} - long-dashed line, $L_X = 10^{42}$ erg s^{-1} - short dashed line, and dotted line - model with no irradiation. The same canonical model (solid line) in panel (c) is compared with the model of $\alpha_X = 0.6$ - short dashed line, and $\alpha_X = 1.2$ - long dashed line. Panel (d) shows the canonical model (solid line), compared with the structures of the atmosphere illuminated by the same radiation: $L_X = 10^{43}$ erg s^{-1} , $\alpha_X = 0.9$, but for Comp. II - short dashed line, and Comp. III - long dashed line. Only first rings are presented for all models in panels (b), (c) and (d).

The transition between hot and cold zone is very steep, geometrically thin, and depends on the initial conditions of a particular ring. For the first ring the transition occurs deeper in an atmosphere than for the outermost eight ring (panel (a)). The shape of the transition is caused by ionization on heavy elements and sometimes possesses small horizontal branch, which is consistent with results from previous photoionization computations (Nayakshin & Kallman 2001). The location of such horizontal branch changes for different chemical compositions as shown in panel (d).

The temperature profile of an irradiated disk causes the ionization structure of the atmosphere to exhibit two dis-

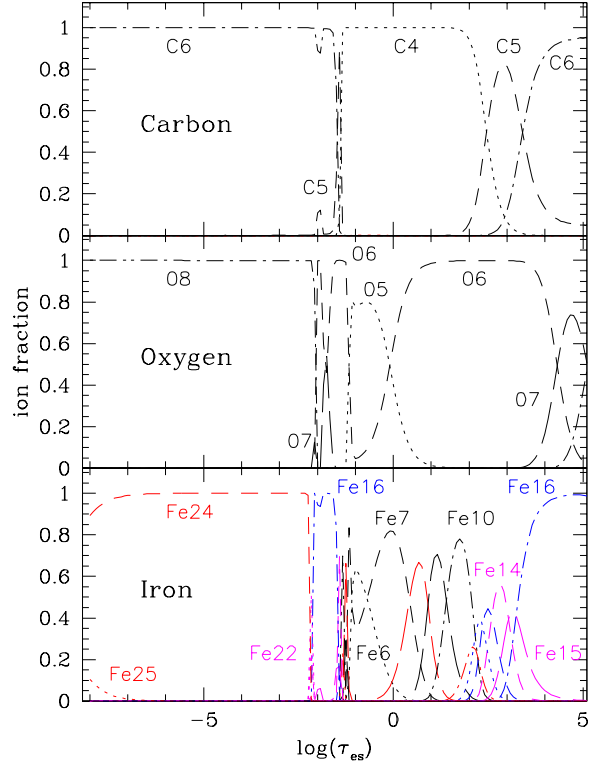


Figure 2. Ionization structure of three main elements for the model with solar chemical composition (Comp. II see Tab. 2). Panel (a) shows ionization fraction of carbon ions, panel (b) - oxygen ions, and panel (c) - iron ions.

Table 3. Description of lines in Figs. 3- 8

type of a line	$\cos(i)$	i
solid black	0.9801	11.4°
short-long dashed	0.8983	26.1°
long dashed dotted	0.7628	40.3°
short dashed dotted	0.5917	53.7°
dotted	0.4083	65.9°
short dashed	0.2372	76.3°
long dashed	0.1017	84.2°
solid red	0.0199	88.9°

tinctly separated regions. The surface high temperature zone is just the region where heavy elements are in highly ionized states. Below that all elements change into low ionization states. We have illustrated this behaviour in Fig. 2, prepared for the ring 1, irradiated by power-law with $\alpha_X = 0.9$ and luminosity $L_X = 10^{43}$ erg s^{-1} , with solar chemical composition, Comp. II, (see: Tab. 2). The ion number denotes the number of missing electrons in particular atom. In the outermost hot layer, oxygen and carbon are completely ionized, while the most abundant iron, Fe24, is in the form of helium-like.

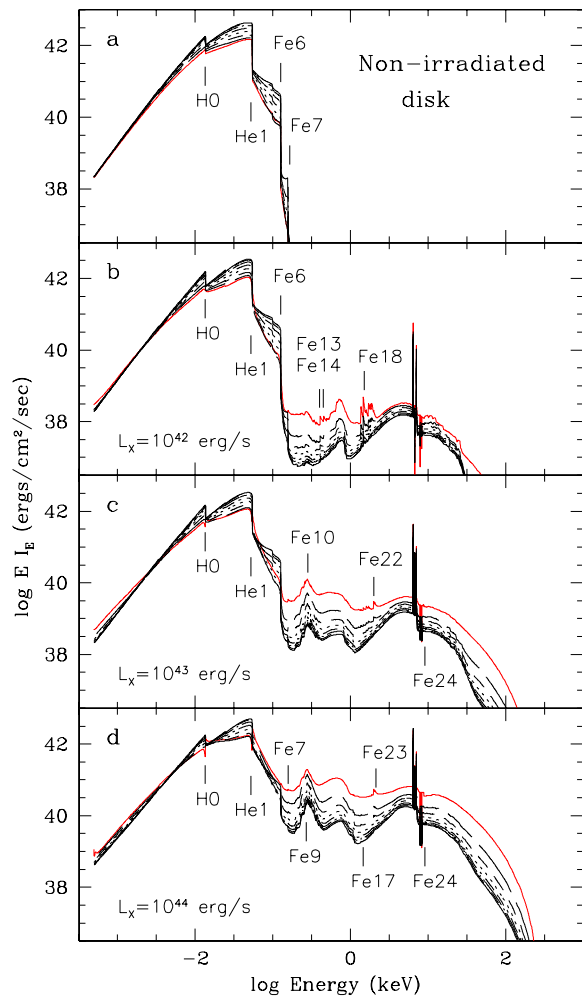


Figure 3. Outgoing spectra from the disk integrated over radii for eight different aspect angles (see Tab. 3). Red solid line represents edge on disk, while black solid line represents disk seen face on. Panel (a) shows spectra of the disk with no irradiation. Panels (b), (c), (d) show models with the same $\alpha_X = 0.9$, but for three different luminosities 10^{42} , 10^{43} and 10^{44} erg s^{-1} , respectively. The most important ions producing the key spectral features have been indicated.

4.2 Outgoing intensity spectra

Figures 3 - 8 present outgoing intensity spectra of the whole accretion disk at various aspect angles. The spectra were obtained by integration over eight rings located at different radii, see Tab. 1. Particular lines in Figs. 3 - 8 correspond to different angles between the direction to the observer and the normal to the disk. Exact values of those eight angles and their cosines are given in Table 3. In further discussion we draw attention of the reader to the extreme angles: solid black line represents almost vertical direction (face-on aspect), whereas the solid red line represents almost horizontal direction (edge-on aspect).

The spectrum of our canonical model is compared with the model of the same spectral index but different X-ray luminosities, Figs. 3, and 6, and of the same X-ray luminosity but different spectral indices Fig. 4, and 7. Spectra for various chemical compositions and the same irradiation are plotted in Figs. 5, and 8.

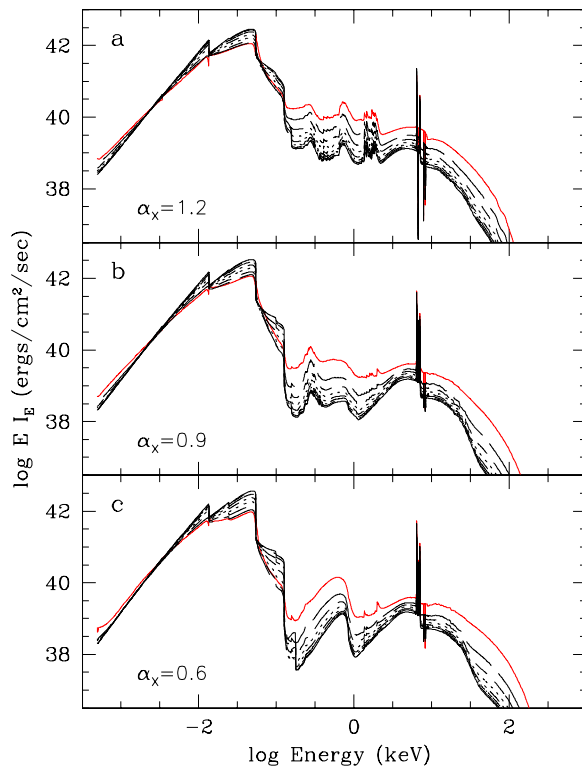


Figure 4. Outgoing spectra from the disk integrated over radii for eight different aspect angles (see Tab. 3). Red solid line represents edge on disk, while black solid line represents disk seen face on. Panels (a), (b), (c) show models with the same $L_X = 10^{43}$ erg s^{-1} , but for three different spectral indices 1.2, 0.9 and 0.6, respectively.

Panel (a) in Fig. 3 presents intensity spectra of the disk with no irradiation. Comparison to panels (b)-(d) shows, that all emerging radiation above 0.2 keV originates from the disk atmosphere as the result of an external hard X-ray illumination.

In all irradiated models outgoing spectra show the effect, that the intensity of radiation emerging almost horizontally to the disk ($i = 88.9^\circ$) is greater than the intensity emerging almost vertically ($i = 11.4^\circ$). This is valid in the X-ray energy band from about 0.1 keV up to 100 keV, and in the infrared band. Such an effect of limb-brightening should be attributed to the inversion of temperature in the irradiated disk atmospheres, see Fig. 1.

All broad-band spectra show the deficit of hard X-rays, which were absorbed in the disk and suffered continuum Compton downscattering. This caused that the energy of hard X-rays was redistributed to lower energies. Moreover, there exists a spectral bump below 1 keV, which is similar to the well known soft X-ray excess. Such bump is more prominent for the disk seen edge on (red solid line) in all models.

5 IRON LINE COMPLEX

External irradiation generates two iron fluorescent lines: K_α doublet at 6.391 and 6.404 keV, and K_β singlet at 7.057 keV.

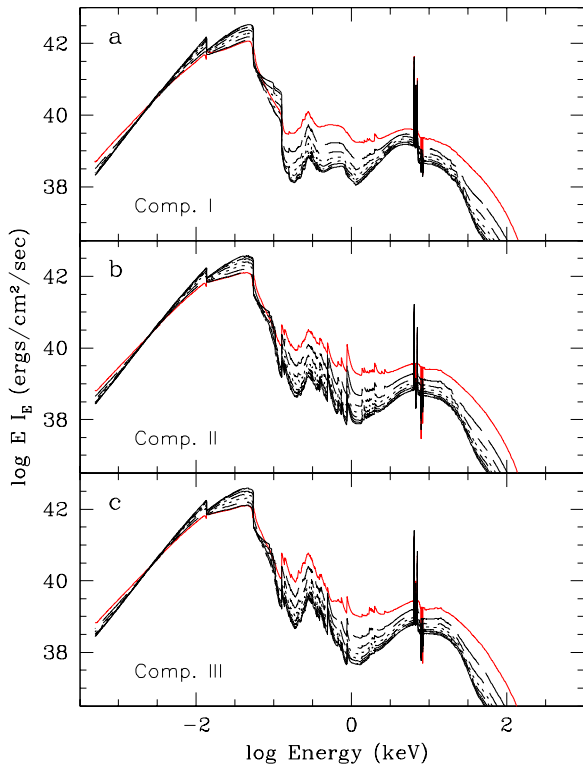


Figure 5. Outgoing spectra from the disk integrated over radii for eight different aspect angles (see Tab. 3). Red solid line represents edge on disk, while black solid line represents disk seen face on. Panels (a), (b), (c) show models with the same $\alpha_X = 0.9$, and $L_X = 10^{43}$ erg s $^{-1}$, but for three different chemical compositions: Comp. I, Comp. II, Comp. III respectively, given in Tab. 2.

Furthermore, due to Compton scattering of the line photons in the irradiated atmosphere photons from line core are shifted toward lower energies creating red wing, which is called Compton shoulder. All the above features are simultaneously reproduced in our model calculations.

Figs. 6, 7, 8 present integrated intensity spectra just around the fluorescent K_α doublet (left panels), Compton shoulder (middle panels), and fluorescent K_β singlet (right panels) for all computed spectra. Unfortunately, Compton shoulder of K_β line is very weak in our models.

Limb-brightening is clearly seen in the region of iron line complex. The Compton shoulder is most prominent in the vertical direction (black solid line), while it almost disappears for the disk seen edge on (red solid line).

The amount of energy emitted by iron line features depends on the shape and luminosity of irradiating continuum and on its spectral index. We have computed equivalent widths of modeled iron line components, and collected them in Table 4 for two extreme aspect angles: face on ($i = 11.4^\circ$) and edge on, $i = 88.9^\circ$. Features are stronger for models with lower luminosity and harder spectral index. For such cases, also K_α and K_β lines seen edge on are more prominent. The energy emitted in Compton shoulder is about ten and more times lower than the energy emitted in K_α line.

5.1 Chemical composition of the accretion disk

Presence of iron atoms in the gas of Comp. I ensures generation of iron K_α and K_β iron fluorescent lines and their Compton Shoulders (Tab. 4 first five rows). Both fluorescent lines originate in deeper (colder) atmospheric layers, where iron atoms are only weakly ionized. However, if the actual chemical composition is rich of various heavy elements, like C, O, Si, S etc., then the appearance and equivalent widths of both fluorescent lines can be reduced due to K-edge absorption of X-ray photons by all those elements.

To check this we have computed disk models for our canonical X-ray luminosity $L_X = 10^{43}$ erg s $^{-1}$ and spectral index $\alpha_X = 0.9$ assuming other chemical compositions (Comp. II and Comp. III) with the excess of helium and the solar chemical abundance of eight heavier elements: C, N, O, Ne, Mg, Si, S and Fe (see Table. 2).

Table. 4 shows that the equivalent widths of the Compton Shoulder has the highest value in models of Comp. I, both for K_α and K_β lines. Addition of heavy elements other than iron (Comp. II, and Comp. III) and their K-edge absorption, significantly decreases EW of Compton Shoulder (compare rows 2, 6 and 7 of Table. 4). The same holds for K_α and K_β line cores seen edge-on. But for the disk seen face-on ($i = 11.4^\circ$), the situation for line cores is opposite. EWs of both line cores increase with addition of heavy elements.

6 DISCUSSION

Calculations of an accretion disk atmosphere irradiated by external hard X-rays are very time consuming and sometimes converge with difficulty. In our paper we have computed the disk up to the distance from the central black hole equal $18R_{Schw}$. Model atmospheres of farther rings did not converge with our computer code. Going farther from the black hole, the gravity in the disk atmosphere becomes lower, and irradiation disturbs hydrostatic equilibrium due to strong radiative pressure. This problem should be solved using dynamical calculations, but none of recently available hydrodynamic codes contains such complicated radiative transfer as presented in this paper.

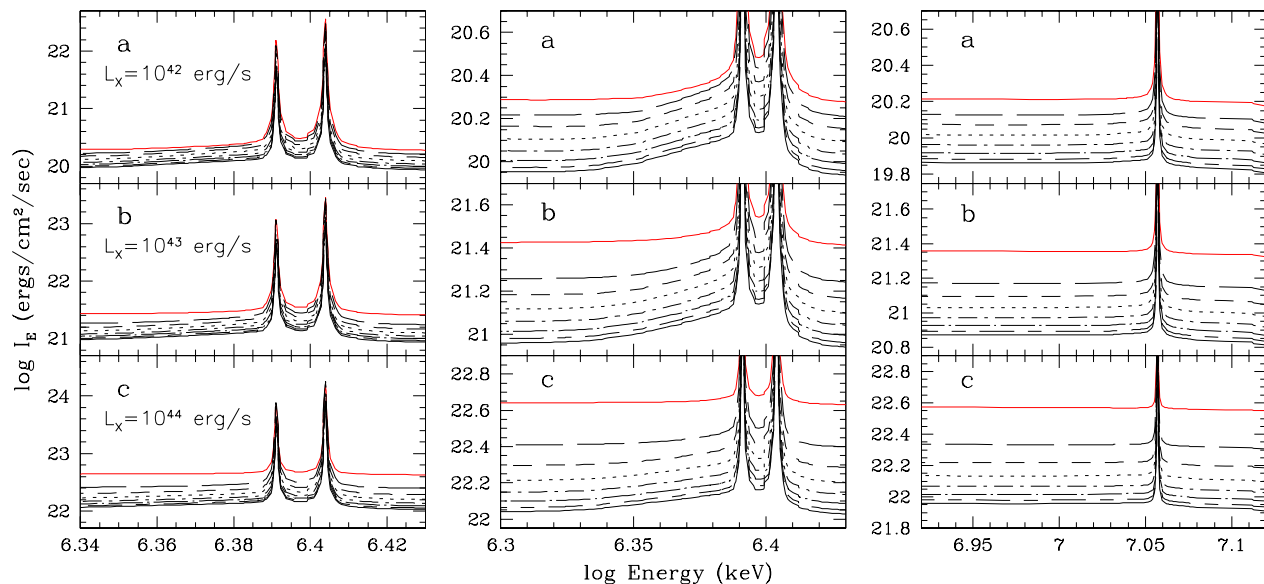
Our treatment of Compton scattering allowed us to compute the structure of the Compton heated skin in an accretion disk atmosphere together with the transition layer down to the deep cold zone (Hubeny et al. 2001). Structure of the transition layer depends on heavy elements abundance. We have shown that the position of a small horizontal branch around 3×10^5 K changes with chemical composition of an irradiated gas.

In the soft X-ray domain of our model spectra we observe huge increase of specific intensity due to Compton redistribution of hard X-ray photons toward lower energies. We claim here, that those bumps give impact to soft X-ray excess frequently observed in many objects. Such excess in our models is higher for higher luminosity of X-ray source and for softer (i.e. higher) power-law index.

All spectra discussed here were computed in the frame of the accretion disk, so we did not consider line broadening and distortion caused by Keplerian motion of gas around black hole. Our goal was to demonstrate the existence of the red wing due to Compton scattering of fluorescent line pho-

Table 4. Equivalent widths of modeled iron line components: K_α , its Compton Shoulder (CS_α), and K_β , and its Compton Shoulder (CS_β). All values are given in eV for two extreme aspect angles: $i = 11.4^\circ$ - face-on, and $i = 88.9^\circ$ - edge-on.

α_X	$\log(L_X)$	Chem.	K_α $i = 11.4^\circ$	K_α $i = 88.9^\circ$	CS_α $i = 11.4^\circ$	CS_α $i = 88.9^\circ$	K_β $i = 11.4^\circ$	K_β $i = 88.9^\circ$	CS_β $i = 11.4^\circ$	CS_β $i = 88.9^\circ$
0.9	42	Comp. I	104.31	211.53	15.34	6.34	15.61	31.68	1.39	0.51
0.9	43	Comp. I	108.18	115.33	12.13	4.36	15.39	16.90	1.24	0.27
0.9	44	Comp. I	68.11	39.44	9.22	2.12	9.58	5.83	0.97	0.18
0.6	43	Comp. I	111.12	144.25	13.33	3.73	15.75	20.85	1.36	0.40
1.2	43	Comp. I	82.66	30.65	6.92	1.55	11.96	4.65	0.76	0.14
0.9	43	Comp. II	125.06	30.10	6.57	1.78	16.67	4.88	0.57	0.06
0.9	43	Comp. III	210.15	67.04	9.88	3.14	27.92	10.89	0.72	0.00

**Figure 6.** Iron line complex in the disk spectra integrated over radii for 8 different aspect angles (see Table 3). Panels (a), (b), and (c) show model spectra with the same $\alpha_X = 0.9$, but for three different luminosities 10^{42} , 10^{43} and 10^{44} erg s $^{-1}$, respectively. Iron K_α doublet is presented in the left panels, whereas Compton shoulder of this line is shown in the middle panels. Right panels show K_β line with Compton shoulders of a marginal height.

tons on a colder electron gas. Narrow K_α lines recently observed by *XMM-Newton* and *Suzaku* satellites have equivalent width 75 eV in case of MCG+8-11-11 (Matt et al. 2006), 165 eV in NGC 2992 (Yaqoob et al. 2007) and 190 eV in the famous object MCG-6-30-15 (Miniutti et al. 2007). Those values of EWs are reproduced by our model calculations, see Table 4. The resolution of actually working satellites is unable to resolve iron K_α double profile.

Similar comparison with K_β line shows excellent agreement of our models with observations. Yaqoob et al. (2007) reported detection of K_β iron line in NGC 2992 with an EW of about 27 eV, and Matt et al. (2006) estimated an upper limit of 10 eV in MCG+8-11-11.

There are not many detections of Compton shoulder in AGN. Most probably, because it is very difficult to distinguish between red wing produced by Compton scattering and that caused by relativistic disk motions. Nevertheless, EW of Compton shoulder fitted by Matt et al. (2006) in MCG+8-11-11 equals 17 ± 10 eV. Such a value agrees with values obtained in our computations for the disk seen face on,

which contains only hydrogen, helium and iron (Comp. I). EW and the profile of Compton shoulder presented in this paper were computed on the basis of detailed model atmosphere calculations, whereas Matt (2002) estimated them from models of irradiated “wall” of constant density.

Our models of broad-band intensity spectra from the irradiated accretion disk are interesting also in other spectral domains, for example in infrared and optical bands. They can be immediately used to study other important spectral features like hydrogen Lyman edge which looks different depending on aspect angle. We address this issue for future consideration.

7 SUMMARY

In this paper we presented intensity spectra emerging from a sample accretion disk around a supermassive black hole in AGN. The disk was irradiated by hard X-rays of the power-law spectral shape originating from a point-like source located above the inner disk. We compared results for the

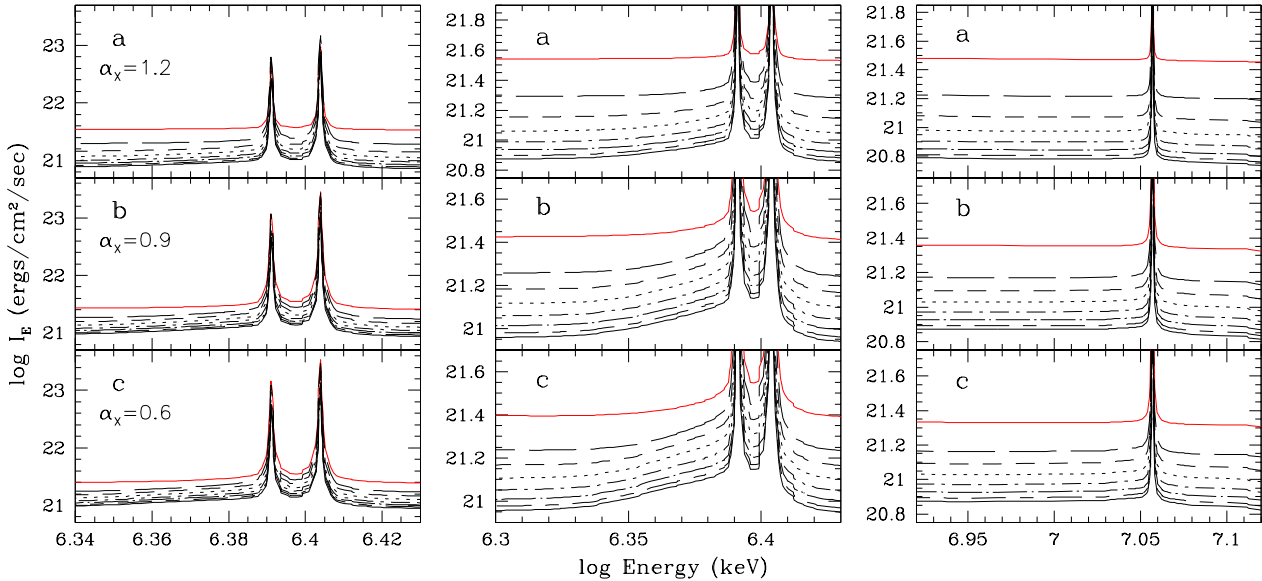


Figure 7. Iron line complex in the disk spectra integrated over radii for 8 different aspect angles (see Table 3). Panels (a), (b), and (c) show model spectra with the same $L_X = 10^{43}$ erg s $^{-1}$, but for three different spectral indices 1.2, 0.9 and 0.6, respectively. Iron K_α doublet is presented in the left panels, whereas Compton shoulder of this line is shown in the middle panels. Right panels show K_β line with very low red-wing Compton shoulders.

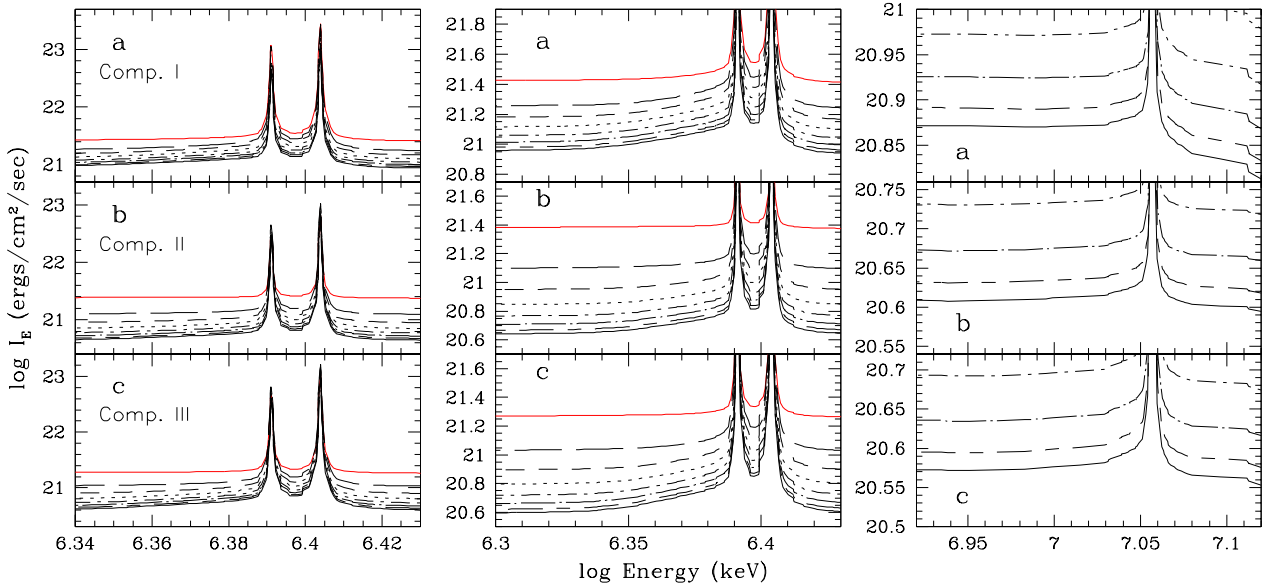


Figure 8. Iron line complex in the disk spectra integrated over radii for 8 different aspect angles (see Table 3). Panels (a), (b), and (c) show model spectra with the same $L_X = 10^{43}$ erg s $^{-1}$, and spectral index $\alpha_X = 0.9$, but for three different chemical compositions, Comp. I, Comp. II, and Comp. III respectively. Iron K_α doublet is presented in the left panels, whereas Compton shoulder of this line is shown in the middle panels. Right panels show enlarged K_β lines with their weak Compton shoulders.

cases when irradiation luminosity, power-law spectral index, and chemical composition change.

Reprocessing of external hard X-rays causes generation of a very hot external layer in the disk atmosphere where temperature rises to millions K, whereas the structure of deeper atmospheric layers is not affected at all.

We numerically reproduced redistribution of external

X-rays both by thermal emission from the heated disk skin and by Compton downscattering in deeper and colder layers of the disk atmosphere. As the result outgoing intensity spectra of the disk exhibit the following important observable properties.

First, external irradiation generates two fluorescent lines of iron, K_α and K_β . Compton scattering of the line

radiation on colder electron gas (below the hot disk skin) generates the Compton shoulder on the red side of both K_α and K_β fluorescent lines, nevertheless shoulder is very weak for K_β line. Compton shoulders modeled here differs from the Compton shoulder presented by Matt (2002), when the latter resulted from X-ray reflection off the constant density slab. Equivalent widths of iron line complex agree with recent observations (Matt et al. 2006; Yaqoob et al. 2007; Miniutti et al. 2007).

Second, Compton scattering of the external X-rays causes build up of the soft X-ray excess below 1 keV. This excess is higher for the disk observed face on, but still too low to explain observations.

Third, our results clearly demonstrate the effect of limb brightening of the disk radiation mostly in the X-ray domain. This result can put new constraints on the geometry of the X-ray source and the reflecting disk atmosphere. We address this issue for further consideration.

ACKNOWLEDGMENTS

This research was supported by the Polish Committee for Scientific Research grant No. N N203 4061 33

REFERENCES

- Ballantyne D. R., Ross R. R., Fabian A. C., 2001, MNRAS, 327, 10
- Basko M. M., 1978, ApJ, 223, 268
- Chaisson E., McMillan S., 1996, Astronomy today. Upper Saddle River, N.J. : Prentice Hall, c1996. 2nd ed.
- Done C., Madejski G. M., Życki P. T., Greenhill L. J., 2003, ApJ, 588, 763
- Fabian A. C., Rees M. J., Stella L., White N. E., 1989, MNRAS, 238, 729
- Guainazzi M., Perola G. C., Matt G., Nicastro F., Bassani L., Fiore F., dal Fiume D., Piro L., 1999, A&A, 346, 407
- Guilbert P. W., 1981, MNRAS, 197, 451
- Hubeny I., Blaes O., Krolik J. H., Agol E., 2001, ApJ, 559, 680
- Iwasawa K., Fabian A. C., Young A. J., Inoue H., Matsumoto C., 1999, MNRAS, 306, L19
- Krause M. O., Oliver J. H., 1979, Journal of Physical and Chemical Reference Data, 8, 329
- Madej J., 1991, ApJ, 376, 161
- Madej J., Różańska A., 2000a, A&A, 356, 654
- Madej J., Różańska A., 2000b, A&A, 363, 1055
- Madej J., Różańska A., 2004, MNRAS, 347, 1266
- Markowitz A., Takahashi T., Watanabe S., Nakazawa K., Fukazawa Y., Kokubun M., Makishima K., Awaki H., Bamba A., Isobe N., 2007, ApJ, 665, 209
- Matt G., 2002, MNRAS, 337, 147
- Matt G., Bianchi S., de Rosa A., Grandi P., Perola G. C., 2006, A&A, 445, 451
- Mihalas D., 1978, Stellar atmospheres /2nd edition/. San Francisco, W. H. Freeman and Co., p. 650
- Miniutti G., Fabian A. C., Anabuki N., Crummy J., Fukazawa Y., Gallo L., Haba Y., Hayashida K., Holt S., 2007, PASJ, 59, 315
- Nandra K., Iwasawa K., 2007, MNRAS, 382, L1
- Nayakshin S., Kallman T. R., 2001, ApJ, 546, 406
- Nayakshin S., Kazanas D., Kallman T. R., 2000, ApJ, 537, 833
- Petrucci P. O., Ponti G., Matt G., Longinotti A. L., Malzac J., Mouchet M., Boisson C., Maraschi L., Nandra K., Ferrando P., 2007, A&A, 470, 889
- Pounds K. A., Nandra K., Stewart G. C., George I. M., Fabian A. C., 1990, Nature, 344, 132
- Reeves J. N., Awaki H., Dewangan G. C., Fabian A. C., Fukazawa Y., Gallo L., Griffiths R., Inoue H., Kunieda H., 2007, PASJ, 59, 301
- Reeves J. N., Nandra K., George I. M., Pounds K. A., Turner T. J., Yaqoob T., 2004, ApJ, 602, 648
- Reynolds C. S., Begelman M. C., 1997, ApJ, 488, 109
- Risaliti G., Bianchi S., Matt G., Baldi A., Elvis M., Fabiano G., Zezas A., 2005, ApJ, 630, L129
- Różańska A., Czerny B., Życki P. T., Pojmański G., 1999, MNRAS, 305, 481
- Różańska A., Dumont A.-M., Czerny B., Collin S., 2002, MNRAS, 332, 799
- Tanaka Y., Nandra K., Fabian A. C., Inoue H., Otani C., Dotani T., Hayashida K., Iwasawa K., Kii T., Kunieda H., Makino F., Matsuoka M., 1995, Nature, 375, 659
- Yaqoob T., Murphy K. D., Griffiths R. E., Haba Y., Inoue H., Itoh T., Kelley R., Kokubun M., Markowitz A., Mushotzky R., Okajima T., Ptak A., Reeves J., Serlemitsos P. J., Takahashi T., Terashima Y., 2007, PASJ, 59, 283
- Yaqoob T., Padmanabhan U., 2004, ApJ, 604, 63